Materials Science and Engineering B 321 (2025) 118559

Contents lists available at ScienceDirect

Materials Science & Engineering B

journal homepage: www.elsevier.com/locate/mseb

Observation of large interlayer magnetoresistance in CVD-grown $PtSe_2$ single-crystal flakes

Yuxin Wang [a], Yuhang Xu [a], Shiyan Zeng [a], Jinxiu Liu [a], Minmin Zhao [a], Chao Tan [a], Zegao Wang [a,*]

[a] College of Materials Science and Engineering, Sichuan University, Chengdu 610065, China

ARTICLE INFO

Keywords:
$PtSe_2$ single-crystal flake
Magnetic property
Ferromagnetic transport
Graphene/$PtSe_2$/Graphene device

ABSTRACT

As an emerging two-dimensional transition metal dichalcogenides (2D TMDCs), platinum diselenide ($PtSe_2$) has excellent properties such as narrow band gap and high carrier mobility, redering it an ideal candidate for spintronic devices. However, magnetic studies are still in their infancy for $PtSe_2$ single-crystal flakes grown by chemical vapour deposition (CVD). Herein, Observation of significant interlayer magnetoresistance (MR) in 2H-$PtSe_2$ single-crystal flakes grown by CVD is reported. By analyzing the magnetic transport properties at low temperatures, both $PtSe_2$ flakes with thicknesses of 23 nm and 141 nm exhibit butterfly-shaped hysteresis, confirming the ferromagnetic properties of 2H-$PtSe_2$. The 23 nm-$PtSe_2$ exhibits a higher maximum |MR| ratio of 2.62 % compared to 141 nm-$PtSe_2$ at 5 K, indicating that the magnetism has a more significant effect on the magnetoresistance of $PtSe_2$ with less layers. This phenomenon is similar to that observed in-plane, suggesting that the magnetic modulation of the intra-layer resistance in $PtSe_2$ is comparable to that of the inter-layer resistance. This study reveals the thickness magnetic properties of CVD-synthesised 2H-$PtSe_2$ and will provide richer theories and insights for future studies of $PtSe_2$-based spintronic devices.

1. Introduction

2D TMDCs have shown great application potential in the fields of flexible electronics, spintronics, and photoelectric detection due to their atomic thickness, lack of dangling bonds on the surface, and wide tunable band gap [1–5]. As a relatively new member of this group, $PtSe_2$ has attracted much attention due to its abundant d-electron number [6] narrower band gap [7,8] and vacancy induced magnetism [9,10]. Currently, various synthesis methods are employed for $PtSe_2$, including thermally assisted conversion (TAC) [11,12] chemical vapor transport (CVT) [13,14], CVD [15,16] etc. $PtSe_2$ usually introduces inherent defects such as inevitable vacancies, edges, and grain boundaries during its growth. While defects are generally considered detrimental to material properties, their presence has been shown to successfully introduce many novel properties in many cases [17–19]. For $PtSe_2$, the complete occupation of t_{2g} state results in the intrinsic flakes with no magnetism, while the presence of surface Pt vacancies leads to the magnetic order, including layer-dependent magnetism and the anomalous Hall effect, etc., which makes it attract more attention in lateral and vertical spin torque devices [3], tunnel reluctance devices and spin valve devices [20]. However, The thickness dependence of the magnetic transport properties in $PtSe_2$ along the in-plane and out-of-plane directions has not been explored. The aim of this study is to prepare $PtSe_2$ flakes with controllable thickness by CVD and to systematically investigate the thickness-dependent differences in magnetic transport anisotropy.

Herein, single-crystal 2H-$PtSe_2$ flakes are synthesized by means of NaCl-assisted CVD and Graphene/$PtSe_2$/Graphene vertical devices are fabricated. The electrical properties of the device in the out-of-plane direction are investigated, as well as the magnetic properties with thickness. High resolution transmission electron microscopy (HRTEM) confirmed the clear interface layer structure in the device, and atomic force microscopy (AFM) determined the thickness of $PtSe_2$ in the device to be 23 nm and 141 nm, respectively. Magnetic transport studies verify the ferromagnetism of $PtSe_2$, with its maximum |MR| decreasing with the number of layers of the material, similar to that of the in-plane device. Conversely, the out-of-plane anisotropic magnetoresistance ratio exhibits a decrease with the number of material layers. These findings provide a promising research platform for the application of $PtSe_2$ in spintronics.

* Corresponding author.
E-mail address: zegao@scu.edu.cn (Z. Wang).

https://doi.org/10.1016/j.mseb.2025.118559
Received 24 April 2025; Received in revised form 15 June 2025; Accepted 25 June 2025
Available online 27 June 2025

2. Experiments

The synthesis of $PtSe_2$ flakes is accomplished through implementation of a molten salt-assisted chemical vapour deposition (CVD) method within a three-zone furnace. This furnace is equipped with a quartz tube. The reactant precursor sources consisted of $PtCl_2$ (Damas-bata, 98 %) powder and Se (Alfa Aesar, 99 %), with NaCl powder serving as an auxiliary agent. The c-plane sapphire substrate is inverted and positioned on a boat of quartz, which is loaded with $PtCl_2$ and NaCl. This quartz boat is then placed in a temperature zone III, while an excess of Se powder is placed in the temperature zone I. The process of growth is ealized under conditions of low pressure in the atmosphere of Ar (34 sccm) and H_2 (6 sccm). The temperature zone I has been configured to an operating temperature of 450 ℃, while Zone III has been preset to 800 ℃. The growth time is 45 min. Finally, the entire CVD device is naturally cooled down. The few-layer graphene with optimized thickness and dimensions was first obtained via mechanical exfoliation and then transferred onto pre-patterned electrode channels using a polycarbonate (PC)-assisted transfer method. The electrodes were fabricated on a SiO_2/Si substrate through standard lithography and electron-beam deposition of platinum (Pt) contacts, followed by sequential cleaning in chloroform, acetone, and isopropanol to remove residual PC.

Next, the surface of the CVD-grown $PtSe_2$ sample was coated with a poly(methyl methacrylate) (PMMA) solution and baked at 150 °C for 3 min. The PMMA film was carefully scratched at the edges and then floated on deionized water. The PMMA-encapsulated $PtSe_2$ flake was subsequently transferred onto a polydimethylsiloxane (PDMS) stamp and finally aligned and placed onto the graphene-covered SiO_2/Si substrate at 120 °C. The sample was then immersed in acetone and heated at 60 °C to completely remove the PMMA layer.Finally, an additional graphene layer was stacked on top of the $PtSe_2$ layer using the same PC-assisted transfer method, ensuring no direct contact between the two graphene layers. To improve electrode contact quality, the device was annealed at 250 °C for 2 h under a mixed argon (200 sccm) and hydrogen (20 sccm) atmosphere. The electrical performance of the device is measured by a Keithley 2614B source meter. Magnetotransport characterization is performed using a Quantum Design Physical Property Measurement System (PPMS, Quantum Design).

3. Results and discussion

Graphene is obtained by mechanically exfoliating bulk graphite crystals onto a SiO_2/Si (001) substrate (285 nm thick SiO_2). A sandwich-type vertical heterostructure was successfully constructed by sandwiching a $PtSe_2$ flake synthesised by CVD between two sheets of graphene, where $PtSe_2$ serves as the channel material and graphene serves

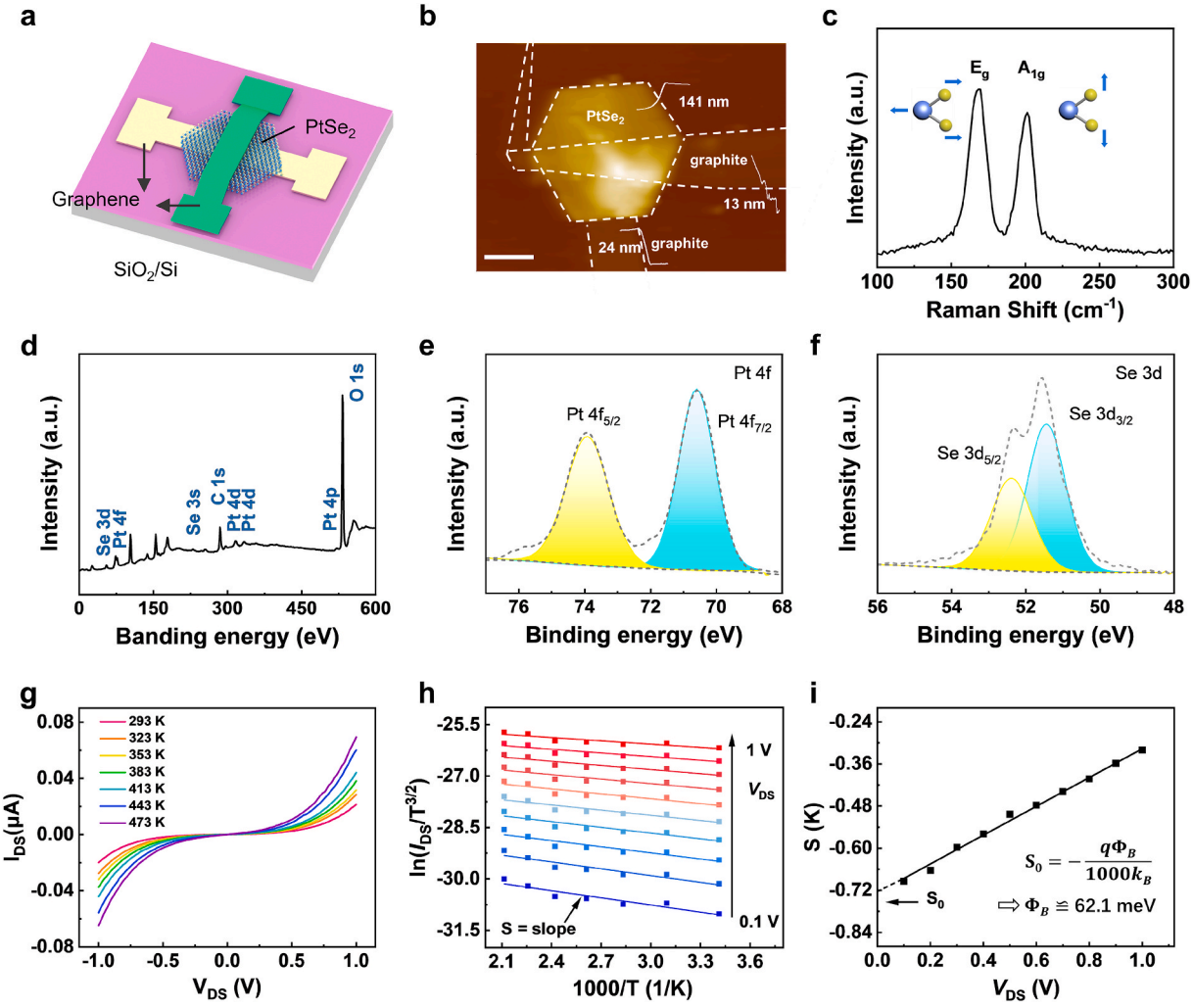

Fig. 1. Morphology and electrical property of Graphene/$PtSe_2$/Graphene device. (a, b) Schematic diagram and AFM height images of Graphene/$PtSe_2$/Graphene device, scale bar, 3 μm. (c) Raman spectrum of $PtSe_2$. High-resolution XPS spectra of (d) full spectrum, (e) Pt 4f, (f) Se 3d. (g) I_{DS}-V_{DS} curves of Graphene/$PtSe_2$/Graphene at 293–473 K. (h) Linear fit of the Arrhenius plot, $\ln(I_{DS}/T^{3/2})$ vs 1000/T. (i) Slopes extracted from Fig. 1e as a function of V_{DS}. Φ_B is derived from the y-intercept, S_0.

as the electrodes. Fig. 1a and 1b show the optical microscope and AFM images of the device, respectively. The thickness of $PtSe_2$ and the graphene are 141 nm, 13 nm and 24 nm, respectively. The $PtSe_2$ flake was characterized by Raman spectroscopy, as shown in Fig. 1c. The flake display two prominent characteristic peaks around 180 cm^{-1} and 210 cm^{-1}, corresponding to in-plane vibrations of Se atoms (E_g mode) and out-of-plane vibrations (A_{1g} mode), respectively. E_g mode intensity is significantly higher than A_{1g} mode, and this difference results from the stronger electron–phonon coupling effect in its in-plane vibration direction. These observations are in agreement with the characteristic peaks of the Raman of multilayered $PtSe_2$ as reported in literature [21,22] The chemical composition of the $PtSe_2$ flakes was characterized by x-ray photoelectron spectroscopy (XPS) (Fig. 1d-1f). The two peaks at 70.6 eV and 73.9 eV correspond to Pt $4f_{7/2}$ and Pt $4f_{5/2}$ of $PtSe_2$, respectively, and the two peaks at 51.45 eV and 52.35 eV correspond to Se $3d_{5/2}$ and $3d_{3/2}$, respectively. The Se/Pt = 1.68 can be derived from the spectrum, which suggests that some selenium vacancies were unavoidably introduced during growth, which is in line with other phenomena in CVD synthesized TMDCs [23,24]. Electrical characterisation was performed by applying a direct bias voltage between the electrodes and recording the current response over a temperature range of 293–473 K. As shown in Fig. 1d, the drain-source current–voltage (I_{DS}-V_{DS}) characteristics of the vertical heterostructure exhibited a pronounced nonlinear transport behaviour. The $PtSe_2$ flake exhibits a distinct contact barrier between the electrodes, attributable to the disparity in the work function of $PtSe_2$ and graphene [25,26]. To investigate contact properties of the device, the Schottky barrier height (Φ_B) of $PtSe_2$ is analysized usi ng the 2D thermionic electron emission model [27–29].

$$I_{DS} = AA^*_{2D}T^{3/2}\exp\left[-\frac{q}{k_BT}\left(\Phi_B - \frac{V_{DS}}{n}\right)\right]$$

The theoretical model contains key parameters such as junction contact area (A), 2D equivalent Richardson constant (A^*_{2D}), magnitude of the electron charge (q), Boltzmann constant (k_B) and ideality factor (n). Notably, instead of the typical Arrhenius plot, ln (I_{DS}/T^2) versus $1000/T$ for three-dimensional (3D) semiconductors, a simplified power law of $T^{3/2}$ for the 2D transport channel was adopted. To determine Φ_B, a plot of ln ($I_{DS}/T^{3/2}$) versus $1000/T$ is constructed for various V_{DS} biases in Fig. 1e. As demonstrated in Fig. 1f, the data are found to be linear at each bias, with the slope (S) plotted as a function of drain-to-source bias. The y-intercept is designated S_0, Φ_B is counted according to the equation $S_0 = -q\Phi_B/(1000k_B)$. For this device, Φ_B is determined to be 62.1 meV. The presence of Φ_B restricts the injection efficiency of electrons from graphene into $PtSe_2$ at low temperatures, resulting in a lower source-drain current. However, as the temperature increases, the number of thermal carriers increases, with some able to overcome the barrier, thus enhancing the injection efficiency and gradually increasing the I_{DS} [30,31]. This result provides a foundation for subsequent magnetic property studies.

To further reveal the structure of the device, cross-sectional image is performed as shown in Fig. 2a. which can be divided into several layers with clear interfaces, including Graphene/$PtSe_2$/Graphene /SiO_2, according to expectations, in which $PtSe_2$ and graphene have a relatively obvious layered structure. High-resolution TEM image and low-pass filtering analysis (Fig. 2b) clearly confirm that the hexagonal structured $PtSe_2$ crystals are in phase 2H [32], exhibiting a characteristic

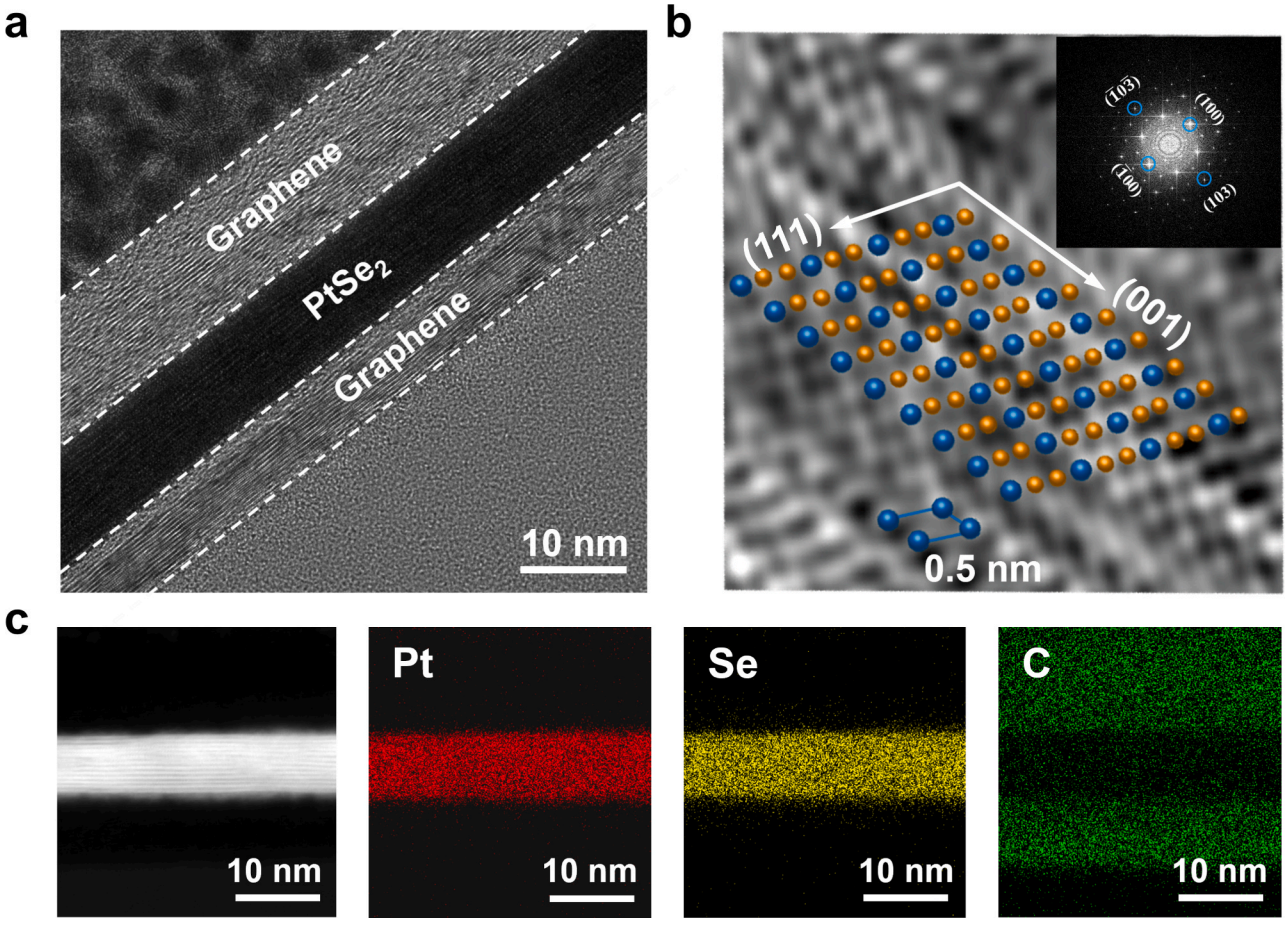

Fig. 2. Structure characteristic of Graphene/$PtSe_2$/Graphene. (a) Cross-sectional HRTEM image. (b) Low-pass filtered TEM image and corresponding crystal model of 2H-$PtSe_2$ crystal. The inset displays the corresponding SAED pattern. (c) EDS mapping pictures of a hexagonal $PtSe_2$ flake and graphene.

lattice spacing of 0.50 nm corresponding to the (001) crystallographic plane of $PtSe_2$. The inset shows a selected area electron diffraction (SAED) map with a sixfold symmetric diffraction spot, further confirming the hexagonal phase structure and single-crystal nature of the hexagonal $PtSe_2$ flake [33]. Furthermore, the corresponding EDS elemental mapping (Fig. 2c) reveals homogeneous spatial distribution of Pt and Se atoms throughout the $PtSe_2$ flakec, with absence of impurity elements.

The above studies reveal the structure and electrical properties of the Graphene/$PtSe_2$/Graphene device, providing a good platform for studying magnetic properties. It is well established that crystal defects introduced during the growth process can induce stable magnetism in $PtSe_2$ [33,34]. However, the magnetic properties of CVD-grown $PtSe_2$ along the out-of-plane direction have never been investigated. To this end, the magnetic transport properties related to the thickness of $PtSe_2$ and the direction of the magnetic field are discussed by applying a vertical magnetic field ranging from −2 T to 2 T. The magnetic resistance (MR) curves from 5 K to 300 K are depicted in Fig. 3a and 3b for $PtSe_2$ vertical devices with thicknesses of 23 nm and 141 nm, respectively. The magnetoresistance (MR) ratio can be calculated by the following formula:

$$MR(\%) = (R - R_0)/R_0$$

where R is the resistance varying with the magnetic field, and R_0 is the resistance at zero magnetic field. The MR curves exhibit butterfly-shaped magnetoresistance hysteresis, indicating that 2H-$PtSe_2$ actually possesses ferromagnetism [10,21]. The significant negative magnetoresistance effect observed in $PtSe_2$ samples with 23 nm and 141 nm thicknesses originates from the formation of a stable spin alignment under a strong magnetic field. This spin alignment effectively suppresses spin disorder and scattering of spin-polarized carriers, thus enhancing the conduction efficiency [21,35]. The more pronounced negative magnetoresistance effect observed at low temperatures stems mainly from the relatively small thermal noise, the consistency of the magnetic domain orientation enhances the localization of the carriers through the domain pinning effect, which allows the Kondo effect to have an impact on the transport, leading to an enhanced negative magnetoresistance effect [36,37]. As the temperature increases, more thermally activated carriers are more likely to overcome the Schottky barrier, which together with the magnetic domain pinning effect explains the negative magnetoresistance effect at low temperatures (Fig. 3c, d) [30,31]. In addition, the magnitude of magnetoresistance variation of the 23 nm-$PtSe_2$ device is larger than that of 141 nm-$PtSe_2$ device, suggesting that fewer layers are more susceptible to magnetic field modulation. As demonstrated in previous studies, the magnitude of the coercive field is closely related to the position of the peak in the MR curve [38,39]. herein, the position of the peak in the MR curve is defined as the coercive field. The magnetization reversal of the $PtSe_2$ devices occur when the applied magnetic field is the coercive field. As demonstrated in previous studies, the magnitude of the coercive field is closely related to the position of the peak in the MR curve. It can be clearly seen that the coercive field of both thicknesses of $PtSe_2$ decreases with increasing temperature, which is consistent with the trend of decreasing magnetism with increasing temperature. Higher coercive field of 23 nm-$PtSe_2$ reflects its stronger magnetic property, which is due to the fact that the thinner-$PtSe_2$ flake, the larger the surface-to-volume ratio, leading to a stronger contribution from the surface Pt vacancies to the magnetic moment. At the same time, the magnetic moments induced by $PtSe_2$ defects are subject to a magnetic quenching effect due to interlayer coupling [20]. Consequently, the magnetic performance of multilayer

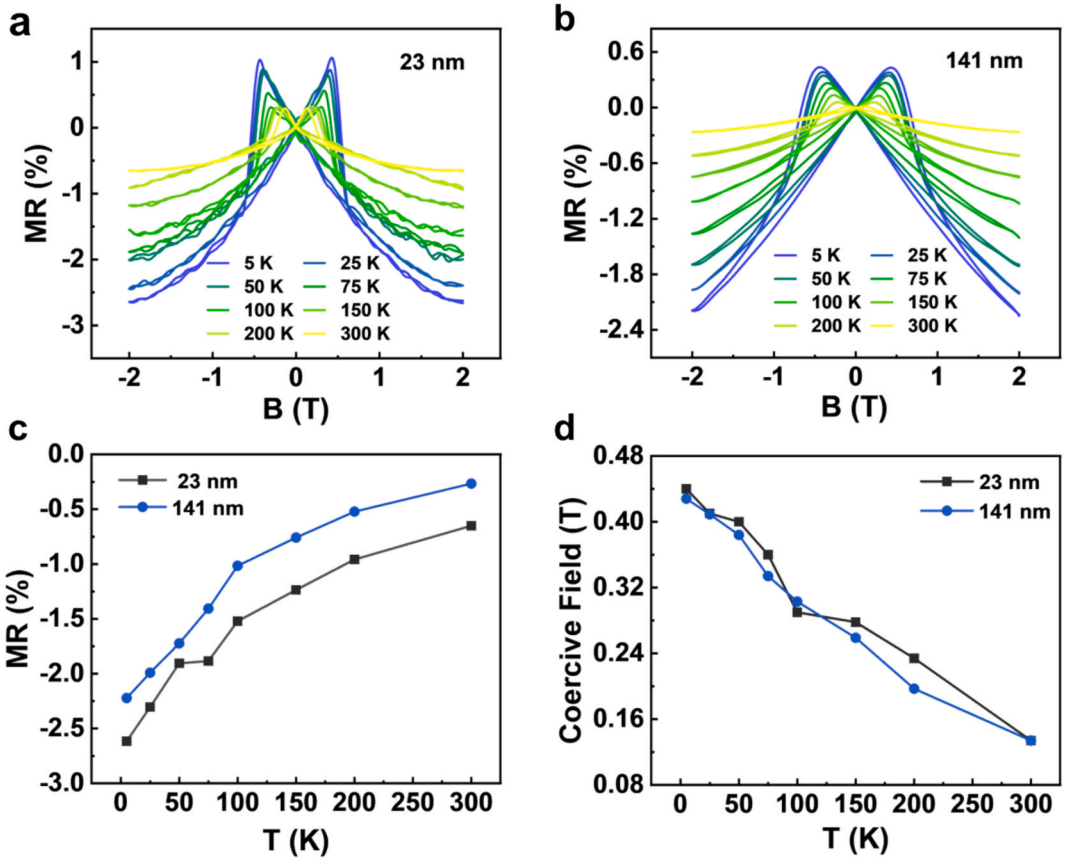

Fig. 3. Magnetoresistance properties of two different thicknesses $PtSe_2$ devices. (a, b) Magnetoresistance curves of (a) 23 nm-$PtSe_2$ and (b) 141 nm-$PtSe_2$ devices at 5 K-300 K. (c, d) The statistical line chart of (c) maximum MR at B = 2T, and (d) the coercive field of two $PtSe_2$ devices of different thicknesses, extracted from (a) and (b).

$PtSe_2$ is significantly lower than that of fewer layers of $PtSe_2$. the maximum |MR| of 23 nm-$PtSe_2$ is always larger than 141 nm-$PtSe_2$, which indicates a more significant modulation of the resistance of the magnet to the thin $PtSe_2$ layer. Furthermore, the temperature dependence of the magnetic properties of 2H-$PtSe_2$ is largely unaffected by thickness regulation. The maximum |MR| of 23 nm-$PtSe_2$ varies from 0.65 % at 300 K to 2.62 % at 5 K, and the coercive field changes from 0.16T at 300 K to 0.47 T at 5 K. The maximum |MR| of 141 nm-$PtSe_2$ varies from 0.27 % at 300 K to 2.22 % at 5 K and coercive field changes from 0.09T at 300 K to 0.43T at 5 K. The nearly identical variation implies that the inter-layer carrier regulation capacities are comparable for the two thicknesses of $PtSe_2$. The maximum |MR| and its variation values at different temperatures are similar to those of the in-plane $PtSe_2$ devices [33], indicating that the magnetic response of $PtSe_2$ is almost the same along the in-plane and out-of-plane directions. This indicates that the magnetic modulation of the internal resistance of the $PtSe_2$ layer is comparable to that of the interlayer resistance.

Magnetic properties of $PtSe_2$ flakes were investigated using a vibrating sample magnetometer with temperature-dependent magnetization measurements. Fig. 4a depicts the magnetization versus temperature curves under a 100 Oe out-of-plane magnetic field. The field-cooled (FC) curve exhibits a monotonic decrease upon heating, whereas the zero-field-cooled (ZFC) curve shows a gradual increase with rising temperature. Crucially, the FC and ZFC branches converge at approximately 300 K, indicating a magnetic transition near room temperature. EDS and XPS analyses exclude the presence of magnetic impurities. Combined with existing theoretical and experimental evidence, these results confirm that the observed ferromagnetism originates from defect-mediated mechanisms in $PtSe_2$. To investigate the anisotropic magnetic transport properties of 2H-$PtSe_2$ synthesized by CVD, the angular dependence of the out-of-plane magnetoresistance of $PtSe_2$ with different thicknesses are investigated. Specifically, a magnetic field of 2 T is applied in the yz plane, and the Graphene/$PtSe_2$/Graphene device is rotated to collect the magnetoresistance under different θ (θ is the angle between the current and the magnetic field). The results reveal angle-dependent MR in $PtSe_2$ flakes of both thicknesses. which demonstrates that the anisotropic nature of the spin current depends on the relative angle between the magnetization direction of the ferromagnet and the charge current direction. As the magnetization direction is rotated relative to the current, spin–orbit coupling modulates the electron scattering probability, consequently changing the resistivity [40,41]. As shown by the hollow circles and squares in Fig. 4, the solid lines are calculated anisotropic magnetoresistance (AMR) curves with $MR = MR_{\perp} + (MR\| - MR_{\perp})\cos^2\theta$, where $MR_{\perp}$ nd $MR\|$ denote the resistance for $\theta = 90^{\circ}$ and $\theta = 0^{\circ}$, respectively, exhibiting consistent angular dependence characterized by a twofold symmetry. The AMR ratios were calculated using the equation:

$$AMRratio = \frac{MR\| - MR_{\perp}}{MR_{\perp}}$$

The calculated AMR ratios of 23 nm-$PtSe_2$ and 141n m-$PtSe_2$ devices are 0.69 % and 0.39 % respectively. The AMR ratio decreases with increasing layer thickness. This phenomenon may be attributed to the dominance of dipole interactions in thicker $PtSe_2$ layers, resulting in smaller width domains being more easily orientated in more than one direction, which enhances the interactions between the domains and thus attenuates the anisotropy of the MR [42,43]. The values of the out-of-plane AMR ratios are similar to those in the in-plane direction [3], further suggesting that the magnetic transfer capacity is similar in the in-plane and out-of-plane directions. The findings collectively demonstrate that the number of layers in $PtSe_2$ significantly influences its angle-dependent spin transport behaviour [44].

4. Conclusion

In summary, the Graphene/$PtSe_2$/Graphene vertical spin device was built on a SiO_2/Si substrate using CVD synthesized $PtSe_2$, and Raman spectroscopy confirmed the high crystalline quality of $PtSe_2$. High resolution characterization confirmed the device structure with the high crystal quality of 2H-$PtSe_2$. Magnetic transport studies revealed that both 23 nm and 141 nm $PtSe_2$ flakes exhibit ferromagnetic properties, while the thinner flake show a higher maximum |MR| of 2.62 % at 5 K. The angular dependence of the MR showed a twofold symmetry, with AMR ratios of 0.69 % and 0.39 % of the 23 nm and 141 nm layers, respectively. Notably, the magnetic response along the out-of-plane direction was similar to that along the in-plane direction, indicating that the modulation of intra- and interlayer carriers in the $PtSe_2$ flakes is comparable under a magnetic field. These findings not only shed new light on the thickness-dependent magnetic properties of 2D materials but also offer valuable insights into the development of high-performance spintronic devices based on $PtSe_2$.

CRediT authorship contribution statement

Yuxin Wang: Writing – original draft, Methodology, Investigation, Conceptualization. **Yuhang Xu:** Investigation, Formal analysis. **Shiyan Zeng:** Methodology, Investigation, Formal analysis. **Jinxiu Liu:** Methodology, Investigation, Formal analysis. **Minmin Zhao:** Methodology, Investigation, Formal analysis. **Chao Tan:** Methodology, Investigation, Formal analysis. **Zegao Wang:** Writing – review & editing, Writing – original draft, Methodology, Investigation, Conceptualization.

Declaration of competing interest

The authors declare that they have no known competing financial

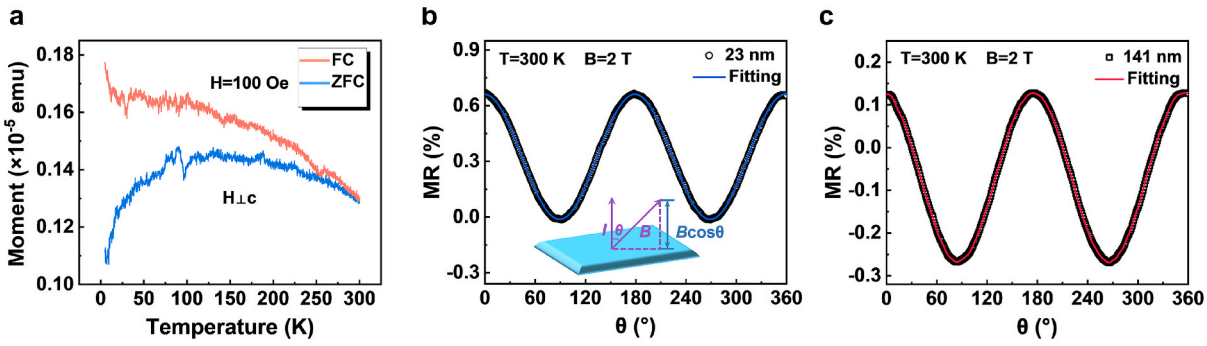

Fig. 4. The magnetic anisotropy of Graphene/$PtSe_2$/Graphene devices. a) Magnetization as a function of temperature for ZFC and FC processes measured under a 100 Oe magnetic field applied perpendicular to the plane. b,c) Angle dependent MR Of 23 nm-$PtSe_2$ and 141 nm-$PtSe_2$ devices at 300 K. Here the angle is measured between the magnetic field and the electric field direction.

interests or personal relationships that could have appeared to influence the work reported in this paper.

Acknowledgements

This work was financially supported by the National Natural Science Foundation of China (52272160, U2330112, 52002254), National Key Research and Development Program of China (2024YFA1209300) and Sichuan Science and Technology Foundation (2023YFSY0002, 2022YFSY0045, 2025YFHZ0102, 2024JDRC0021).

Data availability

Data will be made available on request.

References

[1] T. Akamatsu, T. Ideue, L. Zhou, Y. Dong, S. Kitamura, M. Yoshii, D.Y. Yang, M. Onga, Y. Nakagawa, K. Watanabe, T. Taniguchi, J. Laurienzo, J.W. Huang, Z. L. Ye, T. Morimoto, H.T. Yuan, Y. Iwasa, Science. 372 (2021) 68.
[2] S.H. Choi, S.J. Yun, Y.S. Won, C.S. Oh, S.M. Kim, K.K. Kim, Y.H. Lee, Nat. Commun. 13 (2022) 5.
[3] R. Mudgal, A. Jakhar, P. Gupta, R.S. Yadav, B. Biswal, P. Sahu, H. Bangar, A. Kumar, N. Chowdhury, B. Satpati, B.R.K. Nanda, S. Satpathy, S. Das, P. K. Muduli, Nano Lett. 23 (2023) 1192.
[4] J. Li, X.D. Yang, Z.W. Zhang, W.Y. Yang, X.D. Duan, X.F. Duan, Nat. Mater. 23 (2024) 1326.
[5] Y.G. Zuo, C. Liu, L.P. Ding, R.X. Qiao, J.P. Tian, C. Liu, Q.H. Wang, G.D. Xue, Y. L. You, Q.L. Guo, J.H. Wang, Y. Fu, K.H. Liu, X. Zhou, H. Hong, M.H. Wu, X.B. Lu, R. Yang, G.Y. Zhang, D.P. Yu, E.G. Wang, X.D. Bai, F. Ding, K.H. Liu, Nat. Commun. 13 (2022) 7.
[6] Y.W. Wang, L. Zhou, M.Z. Zhong, Y.P. Liu, S. Xiao, J. He, Nano Res. 15 (2022) 3675.
[7] C. Yim, K. Lee, N. McEvoy, M. O'Brien, S. Riazimehr, N.C. Berner, C.P. Cullen, J. Kotakoski, J.C. Meyer, M.C. Lemme, G.S. Duesberg, ACS Nano 10 (2016) 9550.
[8] J.B. He, X.D. Zhu, W.M. Liu, E.T. Hu, J.L. Wang, R.J. Zhang, Nano Res. 15 (2022) 661.
[9] J. Ge, T.C. Luo, Z.Z. Lin, J.P. Shi, Y.Z. Liu, P.Y. Wang, Y.F. Zhang, W.H. Duan, J. Wang, Adv. Mater. 33 (2021) 7.
[10] A. Avsar, A. Ciarrocchi, M. Pizzochero, D. Unuchek, O.V. Yazyev, A. Kis, Nat. Nanotechnol. 14 (2019) 67.
[11] X. Yang, X. Zhou, L. Li, N. Wang, R. Hao, Y.A. Zhou, H. Xu, Y.T. Li, G.M. Zhu, Z. M. Zhang, J.R. Wang, Q.L. Feng, Small 19 (2023) 9.
[12] J.H. Kim, S. Youn, T.W. Go, J. Kim, C. Yoo, M.S. Shawkat, S.S. Han, S.J. Jeon, Y. Jung, J.Y. Park, W. Lee, Nano Energy 91 (2022) 11.
[13] X.D. Zhu, F.J. Lu, J. Alloy. Compd. 785 (2019) 871.
[14] Y. Huang, Y.H. Pan, R. Yang, L.H. Bao, L. Meng, H.L. Luo, Y.Q. Cai, G.D. Liu, W. J. Zhao, Z. Zhou, L.M. Wu, Z.L. Zhu, M. Huang, L.W. Liu, L. Liu, P. Cheng, K.H. Wu, S.B. Tian, C.Z. Gu, Y.G. Shi, Y.F. Guo, Z.G. Cheng, J.P. Hu, L. Zhao, G.H. Yang, E. Sutter, P. Sutter, Y.L. Wang, W. Ji, X.J. Zhou, H.J. Gao, Nat. Commun. 11 (2020) 1.
[15] Z.G. Wang, Q. Li, F. Besenbacher, M.D. Dong, Adv. Mater. 28 (2016) 10224.
[16] Z.C. Li, M.R. Huang, J. Li, H.W. Zhu, Adv. Funct. Mater. 33 (2023) 9.
[17] X. Wu, H.B. Zhang, J. Zhang, X.W. Lou, Adv. Mater. 33 (2021) 24.
[18] W.H. Niu, S. Pakhira, G.M. Cheng, F. Zhao, N. Yao, J.L. Mendoza-Cortes, B.E. Koel, Nat. Mater. 23 (2024) 1704.
[19] M.L. Zhu, Q.Q. Li, K.W. Guo, B.L. Chen, K. He, C. Yi, P. Lu, X.Y. Li, J.W. Lu, J. Li, R. X. Wu, X.Q. Liu, Y. Liu, L. Liao, B. Li, X.D. Duan, Nano Lett. 24 (2024) 7483.
[20] A. Avsar, C.Y. Cheon, M. Pizzochero, M. Tripathi, A. Ciarrocchi, O.V. Yazyev, A. Kis, Nat. Commun. 11 (2020) 7.
[21] H.F. Ma, Q. Qian, B.A. Qin, Z. Wan, R.X. Wu, B. Zhao, H.M. Zhang, Z.C. Zhang, J. Li, Z.W. Zhang, B. Li, L. Wang, X.D. Duan, Adv. Sci. 9 (2022) 8.
[22] K.A. McComber, X.M. Duan, J.F. Liu, J. Michel, L.C. Kimerling, Adv. Funct. Mater. 22 (2012) 1049.
[23] S. Meng, Y. Yang, X.Y. Dai, Y. Tang, M.F. He, Y.R. Gu, R.B. Jiang, F. Ding, H. Xu, Adv. Funct. Mater. 34 (2024) 9.
[24] X.C. Zhang, L.Y. Zhou, S.P. Wang, T. Li, H.Y. Du, Y.C. Zhou, J.Y. Liu, J.J. Zhao, L. F. Huang, H. Yu, P. Chen, N. Li, G.Y. Zhang, Nat. Commun. 16 (2025) 8.
[25] N. Dimov, A. Staykov, M.I.M. Kusdhany, S.M. Lyth, Nanotechnology 34 (2023) 11.
[26] X. Li, S.E. Wu, D. Wu, T.X. Zhao, P. Lin, Z.F. Shi, Y.T. Tian, X.J. Li, L.H. Zeng, X. C. Yu, InfoMat 6 (2024) 10.
[27] Y. Zhou, W. Han, Y. Wang, F.X. Xiu, J. Zou, R.K. Kawakami, K.L. Wang, Appl. Phys. Lett. 96 (2010) 3.
[28] J.R. Chen, P.M. Odenthal, A.G. Swartz, G.C. Floyd, H. Wen, K.Y. Luo, R. K. Kawakami, Nano Lett. 13 (2013) 3106.
[29] J.E. Seo, M. Gyeon, J. Seok, S. Youn, T. Das, S. Kwon, T.S. Kim, D.K. Lee, J.Y. Kwak, K.B. Kang, J.W. Chang, Adv. Funct. Mater. 34 (2024) 11.
[30] C. Gong, L. Li, Z. L. Li, H. W. Ji, A. Stern, Y. Xia, T. Cao, W. Bao, C. Z. Wang, Y. Wang, Z. Q. Qiu, R. J. Cava, S. G. Louie, J. Xia, X. Zhang and Ieee, San Jose, *Nature*, 2017, **546**, 265.
[31] G.J. Hu, H. Guo, S.H. Lv, L.X. Li, Y.H. Wang, Y.C. Han, L.L. Pan, Y.L. Xie, W.Q. Yu, K. Zhu, Q. Qi, G.Y. Xian, S.Y. Zhu, J.A. Shi, L.H. Bao, X. Lin, W. Zhou, H.T. Yang, H. J. Gao, Adv. Mater. 36 (2024) 9.
[32] L. Xu, L.F. Wang, H. Liu, F. Li, D.L. Li, Y.W. Cao, C.C. Wu, X.D. Bai, J.J. Qi, J. Mater. Chem. C 9 (2021) 5261.
[33] S.Y. Zeng, M.M. Zhao, F. Li, Z.H. Yang, H.J. Wu, C. Tan, Q. Sun, L. Yang, L. Lei, Z. G. Wang, Adv. Funct. Mater. 34 (2024) 10.
[34] J. Klein, Z.G. Song, B. Pingault, F. Dirnberger, H. Chi, J.B. Curtis, R. Dana, R. Bushati, J. Quan, L. Dekanovsky, Z. Sofer, A. Alù, V.M. Menon, J.S. Moodera, M. Loncar, P. Narang, F.M. Ross, ACS Nano 17 (2023) 288.
[35] J.L. Liu, S. Wan, B. Li, B.L. Li, J.Y. Liang, P. Lu, Z.C. Zhang, W. Li, X. Li, Y. Huangfu, R.X. Wu, R. Song, X.D. Yang, C. Liu, R.H. Hong, X.F. Duan, J. Li, X.D. Duan, Nano Lett. 24 (2024) 3768.
[36] C. Gong, L. Li, Z.L. Li, H.W. Ji, A. Stern, Y. Xia, T. Cao, W. Bao, C.Z. Wang, Y. A. Wang, Z.Q. Qiu, R.J. Cava, S.G. Louie, J. Xia, X. Zhang, Nature 546 (2017) 265.
[37] T. Ohta, M. Tokuda, S. Iwakiri, K. Sakai, B. Driesen, Y. Okada, K. Kobayashi, Y. Niimi, AIP Adv. 11 (2021) 5.
[38] H. Matsuoka, S. Kajihara, T. Nomoto, Y. Wang, M. Hirayama, R. Arita, Y. Iwasa, M. Nakano, Sci. Adv. 10 (2024) 8.
[39] T.K. Das, N. Preeyanka, S. Mishra, Y.T. Sang, C. Fontanesi, Adv. Funct. Mater. (2025) 2425377.
[40] V.A. Marsocci, IEEE Trans. Magn. 12 (1976) 46.
[41] W.J. Ci, H.L. Yang, W.H. Xue, R.L. Yang, B.H. Lv, P. Wang, R.W. Li, X.H. Xu, Nano Res. 15 (2022) 7597–7603.
[42] H.X. Wu, J.F. Guo, S. Zhaxi, H. Xu, S. Mi, L. Wang, S.S. Chen, R. Xu, W. Ji, F. Pang, Z.H. Cheng, A.C.S. Appl, Mater. Interfaces 15 (2023) 26148.
[43] W. Zhang, H.T. Guo, J. Jiang, Q.C. Tao, X.J. Song, H. Li, J. Huang, J. Appl. Phys. 120 (2016) 8.
[44] L.J. Meng, Z. Zhou, M.Q. Xu, S.Q. Yang, K.P. Si, L.X. Liu, X.G. Wang, H.N. Jiang, B. X. Li, P.X. Qin, P. Zhang, J.L. Wang, Z.Q. Liu, P.Z. Tang, Y. Ye, W. Zhou, L.H. Bao, H.J. Gao, Y.J. Gong, Nat. Commun. 12 (2021) 8.